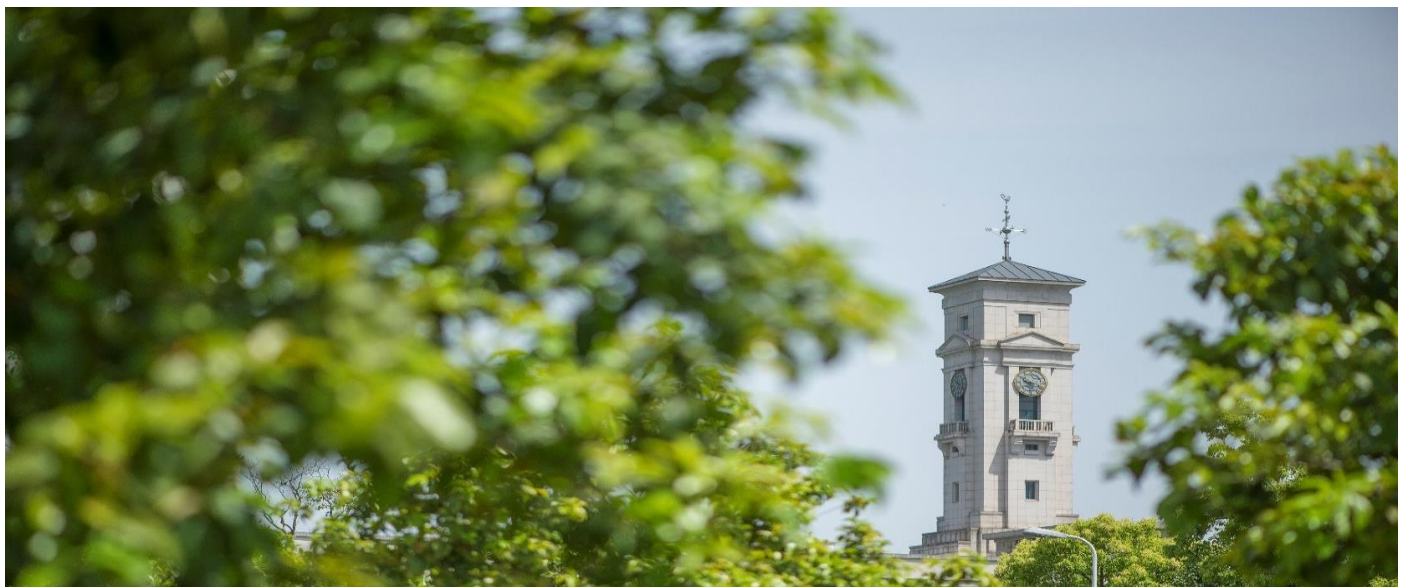# A novel "holey-LFP / graphene / holey-LFP" sandwich nanostructure with significantly improved rate capability for lithium storage

Jiming Lua.[a], Xiaohui Tian.[a], Yingke Zhou.[a], Yanbin Zhu.[a], Zhihao Tang.[a], Ben Ma.[a], Guan Wu.[a], Tingting Jiang.[a], Xiaofeng Tu.[a], George Z. Chen.[a,b]

[b]Energy Engineering Research Group, Faculty of Science and Engineering, University of Nottingham Ningbo China, Ningbo 316100, P. R. China

University of Nottingham

UK | CHINA | MALAYSIA

1

A novel "holey-LFP / graphene / holey-LFP" sandwich nanostructure with significantly improved rate capability for lithium storage

Jiming Lu[a,†], Xiaohui Tian[a,†], Yingke Zhou[a,*], Yanbin Zhu[a], Zhihao Tang[a], Ben Ma[a],

Guan Wu[a], Tingting Jiang[a], Xiaofeng Tu[a], George Z. Chen[a,b]

[a]The State Key Laboratory of Refractories and Metallurgy, Institute of Advanced

Materials and Nanotechnology, College of Materials and Metallurgy, Wuhan

University of Science and Technology, Wuhan 430081, P. R. China.

[b]Energy Engineering Research Group, Faculty of Science and Engineering, University

of Nottingham Ningbo China, Ningbo 316100, P. R. China

[†]These authors contributed equally to this work. [*] Corresponding author. Tel.: +86 2768 862928, Fax: +86 2768 862928. E-mail: zhouyk@wust.edu.cn

1 **Abstract**

2 The development of high-performance and new-structure electrode materials is vital for

3 the wide application of rechargeable lithium batteries in electric vehicles. In this work,

4 we design a special composite electrode structure with the macroporous three-

5 dimensional graphene areogel framework supporting mesoporous $LiFePO_4$ nanoplate.

6 It is realized using a simple sol-gel deposition method. The highly conductivity

7 graphene nanosheets assemble into an interconnected three-dimensional macroporous

8 areogel framework, while $LiFePO_4$ grows along the graphene nanosheets and generates

9 a mesoporous nanoplate structure. In comparison with $LiFePO_4$, this unique sandwich

10 nanostructure offers a greatly increased electronic conductivity thanks to the framework

11 of graphene nanosheets. Also, the bimodal porous structure of the composite

12 remarkably increases the interface between the electrode/electrolyte and facilitates the

13 transport of Li^+ throughout the electrode, enabling the superior specific capacity, rate

14 characteristic and cyclic retention.

15

16 **Keywords:** Sandwich nanostructure, Porous nanoplate, Graphene aerogel, $LiFePO_4$

17

18

19

20

1   **Introduction**

2   New-energy vehicles, such as electric vehicles, are essential to ease the strain on

3   the environment resulting from fast growing consumption of fossil fuels. However,

4   there is still a long way before replacing the traditional vehicles by EVs without

5   commercial losses [1-3]. The main challenge is that the energy/power densities of the

6   current energy storage devices need to increase further to make electric vehicles

7   commercially acceptable and affordable [1, 4-5]. Since the early 1990s, the lithium-ion

8   batteries (LIBs) have been the promising energy-storage devices in terms of capacity,

9   power capability, cycle life and impact on the environment [6-9]. Considerable

10 endeavors have been undertaken to increase the energy/power densities of LIBs by

11 developing novel cell and electrode architectures [10-12]. In general, the

12 electrochemical performance/cost of LIBs depend mainly on the utilized component

13 materials and especially that on the positive electrode [1]. $LiFePO_4$ (LFP) is a

14 competitive candidate for the positive electrode, primarily due to the advantages of high

15 specific capacity, long cycle life, high safety, low price and no poison [13-16].

16 Nevertheless, there are many technical challenges that need to be overcome before LFP

17 can be widely used in the power-type LIBs. The major issues are still the inherently

18 sluggish diffusivity of Li^+ and poor conductivity of electron, both heavily limit the

19 commercial application of LFP [17-18].

1   To solve the transport limitations of ion and electron, numerous works have been

2   reported, including heteroatom doping [18-19], particle size optimizing [20-21] and

3   micro-sturcture design [22-24], and coating with conductive layers (conductive

4   polymer, metal oxide or carbonaceous nanomaterials) [15, 22-26]. These strategies can

5   enhance the Li storage performance of LFP, for instance, when the nanoscale LFP

6   particle is used, an effectively enhanced specific capacity has been demonstrated.

7   However, a nanoscale material usually display the low volumetric energy density and

8   tap density, in addition, the nanomaterial is easy to form agglomerates which result in

9   poor long-term cycling performance [16, 27]. By contrast, LFP nanoplates have

10   recently attracted attention for their good structural stability during cycling and reduced

11   vertical Li^+ transport tunnels [17, 24]. The kinetics of the lithiation/delithiation process

12   is strongly related to the orientation of LFP particles, as the Li^+ migrates along the b-

13   axis of orthorhombic crystal and the transfer of charge occurs primarily on the facet

14   (010). Thus, a controllable growth of (010) facet-oriented nanoplate is anticipated to

15   greatly facilitate the Li-ion transport and increase the electrochemical performance of

16   LFP [17-18, 24].

17   All kinds of carbon materials, including the carbon black, carbon nanotube as well

18   as graphene, are extensively utilized to construct the LFP composites for the

19   improvement of the electronic conductivity [5, 24, 26, 28-30]. Graphene demonstrates

20   a lot of outstanding chemical/physical attributes and possesses intriguing advantages as

21   a conductive reagent for electrode materials, mainly because of the tremendous specific

1   surface area and high conductivity [7, 31-33]. The performances of electrode materials

2   usually enhanced significantly when formed composites with graphene, and it has been

3   reported that LFP/graphene composites displayed even better performance compared

4   to the LFP/carbon black or nanotube composites [15, 23-24]. However, the Hummers

5   method is commonly employed to prepare graphene oxide, and the subquent reduction

6   process usually cause the re-stack of graphene oxide, resulting in substantial decrease

7   of the surface area and deterioration of the utilization efficiency [34]. Recently, the

8   three-dimensional (3D) graphene aerogels (GAs) have been paid a worldwide attention

9   owing to the integration of the 3D hierarchically porous structure as well as the

10   incomparable intrinsic characters of graphene [17, 35-36]. The composites with GA

11   exhibit high porosity and mechanical stability, high ion migration and electron transfer

12   kinetics, which can prevent the re-stack of graphene sheets efficiently [36-37].

13   Therefore, the porous GAs is an ideal matrix to support and modify the electrode

14   materials to greatly increase the electric conductivity and ion diffusion routes [17].

15   Herein, we demonstrate a novel sandwich-like nanocomposite of the mesoporous

16   LFP nanoplates grow along the graphene sheets in a macroporous GA matrix (LFP-

17   GA), as illustrated in Figure 1. In this structure design, the mesoporous LFP nanoplates

18   on both sides of graphene can promote the diffusivity of Li^+, while graphene, the core

19   of sandwich structure, can enhance the charge transfer, to enhance the electrochemical

20   Li-storage performance. The obtained LFP-GA electrode demonstrates excellent

21   specific capacity (162 mAh g^{-1}, 0.1 C), high rate performance (148 and 104 mAh g^{-1} at

1   1 and 10 C) and long cyclic life (capacity retention 80.6 % after 1000 cycles at 1 C),

2   ascribed to the unique characteristics of the composite structure: 1) The GA provides a

3   large surface area to anchor LFP and enable the in-situ formation of LFP nanoplates

4   along the graphene sheets, strengthening the interaction between LFP and GA; 2) GA

5   offers high electronic conductivity and enhances the utilization of LFP on the electrode;

6   3) The 3D interconnected macroporous structures of GA allow the rapid electrolyte

7   permeation inside the electrode; 4) The abundant mesopores in LFP nanoplates

8   generated by the pyrolysis of citric anion can further enlarge the electrode/electrolyte

9   reaction interface, providing more Li^+ diffusion channels.

10   **Experimental**

11   **Synthesis of GAs.** A modified Hummers method was used for the synthesis of

12   graphene oxide (GO) as previous publications [38-40]. GAs were obtained using a

13   hydrothermal process coupled with the subsequent freeze-drying. Typically, aqueous

14   GO solution (2 mg mL^{-1}, 10 mL) was ultrasonically treated for 15 min, before sealing

15   in a hydrothermal reactor and heating for 2 h at 150 °C. The obtained graphene hydrogel

16   was freeze-dried for 48 h to get the GAs.

17   **Preparation of LFP-GA composites.** LFP-GA composites were obtained by using

18   an *in situ* sol–gel method described as follows. Firstly, one solution with 0.01 mol

19   LiH_2PO_4 and 5 mL distilled water, the other solution with 0.01 mol iron (III) citrate and

1   30 mL distilled water, were prepared seperately with stirring, before mixing together

2   and stirring for some time to make the LFP precursor sol. Then, an appropriate amount

3   of the LFP precursor sol was absorbed on a pre-weighed GA and dried in an oven at

4   60 °C to get the LFP gel/GA. Finally, the LFP gel/GA was calcined in a mixed

5   atmosphere (Ar: H_2 =90 : 10) at 600 °C for 5 h to produce the LFP-GA composites.

6   According to the difference in the GA content in the final composites, the obtained

7   samples were marked LFP-GA-x%, where x means the proportion of GA. For

8   comparison, the pristine LFP was synthesized in the absence of GA.

9   **Characterization of materials.** The morphologies and microstructures of LFP and

10 the composites were examined using a field emission scanning electron microscopy

11 (SEM, PHILIPS XL30TMP, 15 kV) and a transmission electron microscopy (TEM, FEI

12 Tecnai G20, 200 kV). The electrodes before and after cycling were washed carefully

13 with tetrahydrofuran and dired before the SEM invesgitations. X-ray diffraction (XRD)

14 was conducted using an Xpert Pro MPD diffractometer (Cu-K_α radiation, λ=0.15418

15 nm) within the 2θ range 15°～85°. Raman spectra were investigated by an IVNIA

16 instrument with a 532 nm argon beam. Thermogravimetry curves (TG) were recorded

17 from 100 °C to 1000 °C (10 °C min^{-1}) in an air atmosphere on the Pyris Diamond

18 instrument (STA449/6/G, NETZSCH). The nitrogen adsorption isothermal curves were

19 obtained on the Autosorb-1-MP/LP analyzer (Quantachrome). The specific surface

20 areas (S_{BET}) was evaluated using the BET method. A VG Multilab 2000 apparatus was

1   used to record the X-ray photoelectron spectroscopy (XPS).

2   **Electrochemical testing.** Electrochemical performance was evaluated using the

3   coin cells on a NEWARE BTS tester (5 V, 50 mA) between 2.5–4.0 V at various

4   charge/discharge rates, in which a Li foil was used as the negative electrode. The

5   working electrode was composed of the active material, super P and polyvinylidene

6   fluoride with a mass ratio of 80:12:8, which were evenly dispersed in N-methyl

7   pyrrolidone to form a slurry and pasted on Al before drying for 10 h at 60 °C. 1 M LiPF$_6$

8   dissolved in EC-DMC (1:1) and polypropylene Celgard 2400 film were used

9   respectively as the liquid electrolyte and separator. The coin cell was fabricated in an

10   argon-filled glove box. An electrochemical workstation (CHI 660D) was used to

11   measure the cyclic voltammetry between 2.5 and 4.2 V and the electrochemical

12   impedance spectroscopy (EIS) from 1 MHz to 100 mHz at a prescribed bias potential

13   of 10 mV.

14   **Results and Discussion**

15   Figure 1 and Figure S1 of the photographs display the procedures to prepare the

16   sandwich-like LFP-GA nanocomposite. Graphene hydrogel is first hydrothermally self-

17   assembled from a GO suspension and then freeze-dried. The LFP colloidal precursor is

18   adsorbed on GA and dried at 60 °C, and then calcined to produce the sandwich

19   nanostructure composited LFP-GA electrode materials. In the synthesis process, the

1   LFP colloidal precursor is absorbed by the 3D interconnected porous framework of

2   graphene aerogel. After drying, the LFP colloidal precursor converts into a gel phase

3   and strongly adhered to the GA skeleton through the possible bonding between the

4   citrate precursor and the remaining oxygen-containing functional groups on graphene

5   after the hydrothermal processing [41]. Finally, the LFP nucleates and grows along the

6   graphene sheets of GA during calcination to form a composite with a 3D macroporous

7   network structure. At the same time, the CO and CO_2 are produced by the thermal

8   degradation of citrate, forming the mesoporous LFP nanoplate structure [29]. The

9   resultant is named LFP-GA-x% according to the ratio of GA, x%. For comparison,

10   pristine LFP was synthesized in the absence of GA.

11   SEM and TEM are used to investigate the morphology and structure of the GA and

12   composites. Figure 2a,b demonstrate an interlaced three-dimensional graphene network

13   of GA, and aboundant interconnected macropores are clearly observed. After deposition

14   of LFP nanoplates (LFP-GA-6%, Figure 2c, 2d), the macroporous aerogel structures

15   are well retained, while the frameworks are covered with LFP nanoplates and become

16   thicker, indicating that the LFP nanoplates have grown along both sides of graphene

17   nanosheets. Such a microstructure can be assigned to the sandwich nanostructure

18   composite model [42,43]. In contrast, the pristine LFP displayed in Figure 2e is denser

19   with a small amount of irregular and discontinued pores, while the LFP-GA-3% sample

20   (Figure 2f) is composed of irregular microsized LFP particles with the graphene

21   nanosheets being hard to inspect, probably due to the overload of LFP, the complete

1 entrapment of graphene nanosheets and the partially filled pores inside the GA matrix.

2 The open, interconnected and continuous macroporous structure of LFP-GA-6% can

3 facilitate the electrolyte infiltration, and the Li^+ transport can be greatly promoted by

4 the highly accessible electrolyte/electrode interface [44].

5   TEM images in Figure 3a and 3b further demonstrate the fine microstructures of

6 LFP-GA-6%. The LFP nanoplates overlay tightly on the graphene based matrix, and

7 abundant mesopores of 20~50 nm in the nanoplates are clearly visible. Formation of

8 these mesopores may be attributed to the citric anion decomposition generated gases

9 and their further expulsion from the inner of LFP particles [29]. Therefore, such a

10 composite can be considered as an interesting bimodal porous electrode material. The

11 interconnected and continuous macroporous GA networks provide plenty of routes for

12 efficient transport of the Li- ions to facilely reach the LFP nanoplates, and the

13 mesopores in the LFP nanoplate can further facilitate the Li^+ transport inside of the

14 active materials, offering fast ion transport kinetics [29-30, 36, 45]. Figure 3c indicates

15 that the LFP nanoplates are tightly covered on both of the top and bottom sides of

16 graphene, forming a LFP-graphene-LFP sandwich-like composite structure. The

17 interplanar spacings of 5.22 Å and 4.71 Å in Figure 3c are respectively associated to

18 the crystal planes of (100) and (001), implying that the nanoplate grows along the (010)

19 plane vertical to the [010] direction [17, 24], which is further proven by the

20 corresponding selected area electronic diffractions (Figure 3d). Such a crystal

21 orientation is believed to benefit shortening the Li^+ diffusion length for its unique one-

1   dimensional transport in the LFP crystal during the insertion/de-insertion processes [17].

2   XRD is used to further identify the crystal structures of the products, and Figure 4

3   depicts that the diffraction patterns of the as-prepared samples can be indexed into a

4   pure-phase orthorhombic LFP (JCPDS No. 83-2092) [24, 46].

5   N_2 adsorption/desorption isotherms of the composites are measured to analyze

6   the bimodal pore characters, and the corresponding results are displayed in Figure 5a.

7   The isotherms display a hysteresis loop, typical feature of the type-IV curve, revealing

8   the mesoporous structure of the samples [46]. The specific surface areas of LFP, LFP-

9   GA-3% and LFP-GA-6% are measured to be 4.2, 24.2 and 36.4 m^2 g^{-1}, and the pore

10   volumes are respectively 0.015, 0.117 and 0.151 cm^3 g^{-1}. LFP-GA-6% displays much

11   higher pore volume and surface area than the other two samples, indicating that the

12   appropriate GA content can effectively enlarge the reaction area of the active material.

13   As shown in Figure S2, the average pore size of 7.7 and 9.5 nm of LFP-GA-3% and

14   LFP-GA-6% is clearly observed, while the macropores of pristine LFP and the

15   composite materials can not be examined correctly because of the analyzer limitation

16   [17]. The previous SEM, TEM and the pore size analyses give clear evidence that the

17   sandwich nanostructure of mesoporous LFP nanoplate and graphene sheet is formed

18   for the LFP-GA-6% composite material. The high porosity and unique structure of LFP-

19   GA-6% is beneficial to storage of plenty of electrolyte and provision of adequate

20   amounts of Li-ions for rapid intercalation into the active materials, thus remarkably

21   enhance the rate performance [36].

1   The thermogravimetric analysis (TGA) (Figure 5b) demonstrates the weight

2   fraction of carbon in LFP-GA-6% is around 11.3% which is about twice of that (5.8%)

3   in LFP-GA-3% as expected, whilst LFP also showed a weight loss of 1.8%. The

4   additional carbon may result from the decomposition and carbonization of citric anion,

5   which may be favorable for further improvement of the local conductive paths in LFP

6   [2]. Raman spectroscopy in Figure 5c shows two bands at respectively 1337 cm^{-1} and

7   1600 cm^{-1}, which correspond to D band of the disorders/defects and G band of the

8   graphitic components in the carbonaceous substances. The I_D/I_G ratio stands for the

9   degree of disordering or graphitization in carbon [10,20]. The I_D/I_G value of LFP-GA-

10   6% is 0.65, much lower than LFP (0.92) and LFP-GA-3% (0.72), indicating the higher

11   graphitization degree of carbon in LFP-GA-6% due to the higher ratio of graphene,

12   which may enhance the electric conductivity of the composites [29]. XPS were further

13   measured to probe the electronic properties of the obtained materials. Figure S3 and

14   Figure 5d display the core level Fe 2p spectra of LFP and the LFP-GA-6% composite,

15   and the components are fitted and calculated. Because of the coupling of the spin-orbit,

16   two peaks related to Fe $2p_{3/2}$ (709.9 eV) and Fe $2p_{1/2}$ (723 eV) are observed for the Fe

17   2p spectrum, and the corresponding satellite peaks appear at around 713.5 eV and 727

18   eV [22]. In comparision to LFP, the ratio of the Fe $2p_{3/2}$ peak for LFP/GA is increased

19   (56.59% to 63.16%), while the ratio of the Fe $2p_{1/2}$ is decreased (24.64% to 22.08%),

20   which might be originated from the electronic interaction between GA and LFP in the

21   LFP/GA composite. As the LFP nanoplates grow in-situ along the graphene nanosheets

1 and are tightly connected with graphene in GA, there might be strong electronic

2 interactions between LFP and GA because of the unique electronic properties of

3 graphene, leading to the modified spin-orbit coupling or valence state of the Fe element

4 [47]. These results indicate the possible electron transfer and bonding between the GA

5 skeleton and $LiFePO_4$ nanoplate, and which might be a benefical interaction to enhance

6 cycling stability of the composite electrode structure.

7   The coin cells are assembled to evaluate the Li storage properties of the LFP-GA

8 composites, and the typical charge/discharge performances at 0.1 C are shown in Figure

9 6a. The charge/discharge plateau appears at $\sim$3.45 V for all the materials, which is

10 attributed to the $FePO_4/LiFePO_4$ conversion [24]. The discharge specific capacities at

11 0.1 C are respectively 109, 140 and 162 mAh g^{-1} for LFP, LFP-GA-3% and LFP-GA-

12 6%. The remarkable improved specific capacity of the LFP-GA-6% electrode may be

13 ascribed to the bimodel composite structure of macro-porous GA and meso-porous LFP,

14 which can effectively increase the electrode/electrolyte interface area and improve the

15 utilization of active material. From an enlarged area depicted in Figure 6a, the plateaus

16 potential intervals of LFP, LFP-GA-3% and LFP-GA-6% are respectively 58.3, 56.4

17 and 41.5 mV. Curves of LFP-GA-6% charging/discharging at different rates are

18 displayed in Figure 6b (curves of LFP and LFP-3% are respectively shown in Figure

19 S4a and S4b for comparison). The electrode exhibits specific capacities of 148 and 104

20 mAh g^{-1} at 1 and 10 C, corresponding to respectively 92.1% and 64.2% of the initial

21 capacity (0.1 C). Shown in Figure 6c is the comparison of rate performance for LFP

1 and the composites at various rates. Compared to LFP and LFP-GA-3%, LFP-GA-6%

2 displays much higher discharge capacities at a low rate, and at high rates the superior

3 rate characteristics of LFP-GA-6% are even clearer. LFP and LFP-GA-3% display the

4 discharge specific capacities of respectively 46 and 138 mAh g^{-1} at 1 C, much lower in

5 comparison to LFP-GA-6% (148 mAh g^{-1}), indicating the greatly increased rate

6 capability of LFP-GA-6% due to the high electronic conductivity GA network and the

7 3D interconnected macroporous/mesoporous structures, which remarkably increase the

8 transport channels for rapid electronic transfer and Li$^+$ diffusion. When the active

9 material loading increases from 1.2 to 1.8 mg, only a slight decrease of specific capacity

10 is observed (~5 mA h g^{-1} from 0.1 to 10 C), indicating the superior rate characteristics

11 and capacity of the LFP-GA-6% electrode even at high loading. The Li storage

12 performances of LFP-GA-6% are also superior in comparison to the porous LFP

13 composites synthesized by the sol-gel method reported in the literature, for example

14 LFP/RuO$_2$ (143 and 92 mAh g^{-1}) [25], LFP/N-CNTs (140 and 50 mAh g^{-1}) [28] and

15 LFP/Graphene (146 and 45 mAh g^{-1}) [29], and the similar freeze-drying synthesized N-

16 CNT incorporated porous LFP (159 and 72 mAh g^{-1}) [22] and mesoporous carbon

17 modified commercial LFP (155 and 58 mAh g^{-1}) at similar charge-discharge rates [48].

18 These results indicate that the GA porous matrix provides the facile 3D ion diffusion

19 route and high electric conductivity, enabling the rapid ion and electron transports and

20 therefore the remarkable high rate characteristic of LFP. The LFP-GA-6% composite

21 electrode is furhter cycled at 1 C for over 1000 cycles to investigate the cycling stability

14

1 (Figure 6d), and the specific capacity remains 119 mAh g^{-1}, 80.6% of its initial

2 discharge specific capacity. Cyclic performances of LFP-GA-6% and LFP-GA-3% are

3 also evaluated at a higher rate of 10 C, as displayed in Figure S5. After 500 cycles at

4 10 C, the LFP-GA-6% composite remains a specific capacity of 100 mAh g^{-1} (96.6%

5 retention), greatly higher in comparison to those of LFP-GA-3% (33 mAh g^{-1}, 80.4%)

6 and LFP (a negligible specific capacity at 10 C), indicating the significantly improved

7 rate and cyclic performance of LFP-GA-6%. The excellent cyclic capability may be

8 associated with the stable structure of the LFP nanoplates *in-situ* grown along the 3D

9 interconnected graphene nanosheets and the strong interactions between the LFP

10 nanoplate and GA network [29], which can be proved from the electrode microstructure

11 for LFP-GA-6% before and after cycling, as displayed in Figure S6a and S6b. As

12 displayed in the images, before cycling the LFP-GA-6% electrode shows a continuous

13 macroporous aerogel structure (Figure S6a), and the original morphology is almost

14 retained after the long-term cycling (Figure S6b). In addition, some fine carbon black

15 particles added during the electrode preparation process are also observed on the

16 surface. In contrast to the previously reported GA supporting LiFePO$_4$ nanoparticle

17 composite [35], the sandwich LFP-GA composite display a slightly lower specific

18 capacity and rate capability, but higher cyclic performance, and further optimizations

19 of the composition and structure, such as the ratio of LFP and GA, the thickness of LFP

20 nanoplate, and the pore size and porosity, would bring even higher overall performance.

21   The cyclic voltammograms are recorded to analyze the reversibility of the LFP

1   materials. As displayed in Figure 6e, all the electrodes possess a couple of

2   anodic/cathodic peaks at 3.6/3.3 V, ascribed to the delithiation/lithiation processes of

3    $LiFePO_4/FePO_4$ [24]. The LFP-GA-6% electrode displays smaller potential gap and

4   higher peak current density compared to LFP and LFP-GA-3%, implying the enhanced

5   electrochemical reaction reversibility and decreased polarization of this electrode. The

6   porous LFP-GA-6% composite structures are favorable to enlarge the solid-liquid

7   reaction interface, increase the Li^+ diffusion channels and promote the ion and electron

8   transports, thus decreasing the polarization of the electrode and increasing the active

9   material utilization and specific capacity. The superior stability and reversibility of

10   LFP-GA-6% can be further proved from the CVs shown in Figure S4c. Figure 6f shows

11   the electrochemical impedance spectra (EIS) of LFP and the composites, which are

12   fitted on basis of the equivalent circuit in the inset. The R_s component represents the

13   electrode/electrolyte ohmic resistance [15], the high-frequency semicircles are ascribed

14   to the electrode/electrolyte charge transfer resistance (R_{ct}) and the capacitance of the

15   double layer (CPE), and the low-frequency straight lines correspond to the Li^+

16   migration related Warburg resistance (Z_w) [1, 15]. Table S2 displays that the fitted R_s

17   and R_{ct} values of LFP-GA-6% are much lower than LFP and LFP-GA-3%, implying a

18   remarkably increased transport kinetics of electron and Li^+ resulted from the synergistic

19   promotion effects of the bimodal porous structures and the graphene aerogel. According

20   to the Warburg region, the diffusion coefficients of Li^+ (D) are calculated with the

21   formula (1) [1, 24]:

$$D = \frac{R^2 T^2}{2A^2 n^4 F^4 C^4 \sigma^2} \qquad (1)$$

where *R, T, A, n,* F, *C* respectively represent the gas constant, absolute temperature, surface area of the cathode, charge transfer number of, Faraday constant, Li^+ concentration, and σ is the Warburg factor related to the angular frequency ω and the imaginary impedance ($-Z_{im}/\Omega$) based on the formula (2) [15, 18]:

$$-Z_{im} = k + \frac{\sigma}{\sqrt{\omega}} \qquad (2)$$

σ is calculated after fitting the curves in Figure S4d (listed in Table S2), then based on formula 2, the obtained D values of Li^+ are respectively 6.76×10^{-15}, 6.55×10^{-14} and 2.04×10^{-13} cm^2 s^{-1} for LFP, LFP-GA-3% and LFP-GA-6%. These results reveal the greatly increased Li^+ transport kinetic of the LFP-GA-6% electrode, attributed to the large reaction interface and the facile Li^+ transport channels in the bimodal porous structures.

Conclusions

A unique bimodal macro/meso-porous LFP nanoplate composites based on the interconnected graphene aerogel frameworks. The LFP nanoplates grow *in-situ* along the graphene nanosheets and form a 3D continuous porous architecture, which facilitate the electrolyte penetration, enlarge the solid/liquid reaction interface, and offer facile channels for charge transport and Li^+ diffusion. As a result, such unique composite exhibits excellent electrochemical capacity, rate and cycling characteristic, which is a promising cathode material of rechargeable lithium batteries. The novel material design

17

and the facile preparation route may be applied to synthesize other high-performance graphene aerogel composite electrode structures, for wide applications in batteries, supercapacitors, and fuel cells, etc.

Supporting Information

Supporting Information Available: additional characterizations, including digital photograph, pore-size distributions, XPS spectrum, discharge curves, CV curves, fitting curves of EIS, cyclic performance, SEM images.

References

1. Y. Zhou, J. Wang, Y. Hu, R. O'Hayre, Z. Shao. A porous LiFePO$_4$ and carbon nanotube composite. Chem. Commun. 46 (2010) 7151-7153.

2. J. Wang, X. Sun. Olivine LiFePO$_4$: The remaining challenges for future energy storage. Energy Environ. Sci. 8 (2015) 1110-1138.

3. J. Lu, Z. Chen, Z. Ma, F. Pan, L. A. Curtiss, K. Amine. The role of nanotechnology in the development of battery materials for electric vehicles. Nat. Nanotechnol. 12

(2017) 1031-1038.

4. Y. Zheng, T. Zhou, X. Zhao, W. K. Pang, H. Gao, S. Li, Z. Zhou, H. Liu, Z. Guo. Atomic interface engineering and electric‑field effect in ultrathin Bi_2MoO_6 nanosheets for superior lithium ion storage. Adv. Mater. 29 (2017) 1700396.

5. J. Mun, H. W. Ha, W. Choi. Nano $LiFePO_4$ in reduced graphene oxide framework for efficient high-rate lithium storage. J. Power Sources 251 (2014) 386-392.

6. D. Li, H. Wang, H. K. Liu, Z. Guo. A new strategy for achieving a high performance anode for lithium ion batteries—encapsulating germanium nanoparticles in carbon nanoboxes. Adv. Energy Mater. 6 (2016) 1501666.

7. Y. Teng, H. Zhao, Z. Zhang, Z. Li, Q. Xia, Y. Zhang, L. Zhao, X. Du, Z. Du, P. Lv. MoS_2 nanosheets vertically grown on graphene sheets for lithium-ion battery anodes. ACS Nano. 10 (2016) 8526-8535.

8. Y. Liu, Z. Tai, T. Zhou, V. Sencadas, J. Zhang, L. Zhang, K. Konstantinov, Z. Guo, H. K. Liu. An all‑integrated anode via interlinked chemical bonding between double‑shelled–yolk‑structured silicon and binder for lithium‑ion batteries. Adv. Mater. 29 (2017) 1703028.

9. J. Hao, J. Zhang, G. Xia, Y. Liu, Y. Zheng, W. Zhang, Y. Tang, W. K. Pang, Z. Guo. Heterostructure manipulation via in-situ localized phase transformation for high-rate and highly durable lithium ion storage. ACS Nano (2018) 10430-10438.

10. M. Armand, J.-M. Tarascon. Building better batteries. Nature 451 (2008) 652-657.

11. A. Vu, Y. Qian, A. Stein. Porous electrode materials for lithium-ion batteries-how

to prepare them and what makes them special. Adv. Energy Mater. 2 (2012) 1056-1085.

12. H. B. Lunghao, F. Y. Wu, C. T. Lin, A. N. Khlobystov, L. J. Li. Graphene-modified LiFePO$_4$ cathode for lithium ion battery beyond theoretical capacity. Nat. Commun. 4 (2013) 1687-1694.

13. W.-J. Zhang. Structure and performance of LiFePO$_4$ cathode materials: A review. J. Power Sources 196 (2011) 2962-2970.

14. G. Wu, Y. Zhou, Z. Shao. Carbon nanotube and graphene nanosheet co-modified LiFePO$_4$ nanoplate composite cathode material by a facile polyol process. Appl. Surf. Sci. 283 (2013) 999-1005.

15. J. Lu, Y. Zhou, T. Jiang, X. Tian, X. Tu, P. Wang. Synthesis and optimization of three-dimensional lamellar LiFePO$_4$ and nanocarbon composite cathode materials by polyol process. Ceram. Int. 42(1) (2016) 1281-1292.

16. J. Lu, Y. Zhou, X. Tian. Research progress of porous lithium iron phosphate. Rare Metal Mat. and Eng. 7 (2017) 2327-2344.

17. B. Wang, W. Al Abdulla, D. Wang, X. S. Zhao. A three-dimensional porous LiFePO$_4$ cathode material modified with a nitrogen-doped graphene aerogel for high-power lithium ion batteries. Energy Environ. Sci. 8(3) (2015) 869-875.

18. B. Wang, A. Liu, W. Al Abdulla, D. Wang, X. S. Zhao. Desired crystal oriented LiFePO$_4$ nanoplatelets in situ anchored on a graphene cross-linked conductive network for fast lithium storage. Nanoscale 7 (2015) 8819-8828.

1　doi:10.1039/C5NR01831E

2　19. M. Chen, L. L. Shao, H. B. Yang, T. Z. Ren, G. Du, Z. Y. Yuan. Vanadium-doping

3　　of LiFePO$_4$/carbon composite cathode materials synthesized with

4　　organophosphorus source. Electrochim. Acta 167 (2015) 278-286.

5　20. K. Kai, Y. Kobayashi, H. Miyashiro, G. Oyama, S. Nishimura, M. Okubo, A.

6　　Yamada. Particle-size effects on the entropy behavior of a LiFePO$_4$ electrode.

7　　ChemPhysChem. 15 (2014) 2156-2161.

8　21. A. Paolella, G. Bertoni, S. Marras, E. Dilena, M. Colombo, M. Prato, A. Riedinger,

9　　M. Povia, A. Ansaldo, K. Zaghib. Etched colloidal LiFePO$_4$ nanoplatelets toward

10　　high-rate capable li-ion battery electrodes. Nano Lett. 14 (2014) 6828-6835.

11　22. X. Tu, Y. Zhou, Y. Song. Freeze-drying synthesis of three-dimensional porous

12　　LiFePO$_4$ modified with well-dispersed nitrogen-doped carbon nanotubes for high-

13　　performance lithium-ion batteries. Appl. Surf. Sci. 400 (2016) 329-338.

14　23. X. Tu, Y. Zhou, X. Tian, Y. Song, C. Deng, H. Zhu. Monodisperse LiFePO$_4$

15　　microspheres embedded with well-dispersed nitrogen-doped carbon nanotubes as

16　　high-performance positive electrode material for lithium-ion batteries. Electrochim.

17　　Acta. 222 (2016) 64-73.

18　24. Y. Zhou, J. Lu, C. Deng, H. Zhu, G. Z. Chen, S. Zhang, X. Tian. Nitrogen-doped

19　　graphene guided formation of monodisperse microspheres of LiFePO$_4$ nanoplates

20　　as the positive electrode material of lithium-ion batteries. J. Mater. Chem. A. 4

21　　(2016), 12065-12072

25. Y. S. Hu, Y. G. Guo, R. Dominko, M. Gaberscek, J. Jamnik, J. Maier. Improved electrode performance of porous $LiFePO_4$ using ruo2 as an oxidic nanoscale interconnect. Adv. Mater. 19 (2007) 1963-1966

26. J. Lu, Y. Zhou, X. Tian. Research progress of nitrogen-doped nanocarbon modified $LiFePO_4$ positive electrode materials. Rare Metal Mat. and Eng. 46 (2017) 2744-2752.

27. C. Nan, J. Lu, L. Li, L. Li, Q. Peng, Y. Li. Size and shape control of $LiFePO_4$ nanocrystals for better lithium ion battery cathode materials. Nano Res. 6 (2013) 469-477.

28. J. Yang, J. Wang, X. Li, D. Wang, J. Liu, G. Liang, M. Gauthier, Y. Li, D. Geng, R. Li. Hierarchically porous $LiFePO_4$/nitrogen-doped carbon nanotubes composite as a cathode for lithium ion batteries. J. Mater. Chem. 22 (2012), 7537-7543.

29. J. Yang, J. Wang, D. Wang, X. Li, D. Geng, G. Liang, M. Gauthier, R. Li, X. Sun. 3d porous $LiFePO_4$/graphene hybrid cathodes with enhanced performance for li-ion batteries. J. Power Sources 208 (2012) 340-344.

30. M. Liu, Y. Zhao, S. Gao, Y. Wang, Y. Duan, X. Han, Q. Dong. Mild solution synthesis of graphene loaded with $LiFePO_4$-C nanoplatelets for high performance lithium ion batteries. New J. Chem. 39 (2015) 1094-1100.

31. X. Liu, T. Xu, Y. Li, Z. Zang, X. Peng, H. Wei, W. Zha, F. Wang. Enhanced x-ray photon response in solution-synthesized $CsPbBr_3$ nanoparticles wrapped by reduced graphene oxide. Sol. Energ. Mat. Sol. C. 187 (2018) 249-254.

32. J. Wei, Z. Zang, Y. Zhang, M. Wang, J. Du, X. Tang. Enhanced performance of light-controlled conductive switching in hybrid cuprous oxide/reduced graphene oxide (Cu_2O/RGO) nanocomposites. Opt. lett. 42(5) (2017) 911-914.

33. Z. Zang, X. Zeng, M. Wang, W. Hu, C. Liu, X. Tang. Tunable photoluminescence of water-soluble aginzns–graphene oxide (GO) nanocomposites and their application in-vivo bioimaging. Sensors and Actuators B: Chemical. 252 (2017) 1179-1186.

34. F. Zhang, X. Yang, Y. Xie, N. Yi, Y. Huang, Y. Chen. Pyrolytic carbon-coated si nanoparticles on elastic graphene framework as anode materials for high-performance lithium-ion batteries. Carbon 82 (2015) 161-167.

35. Z. S. Wu, S. Yang, Y. Sun, K. Parvez, X. Feng, K. Müllen. 3D nitrogen-doped graphene aerogel-supported Fe_3O_4 nanoparticles as efficient electrocatalysts for the oxygen reduction reaction. J. Am. Chem. Soc. 134 (2012) 9082-9085.

36. X. Tian, Y. Zhou, X. Tu, Z. Zhang, G. Du. Well-dispersed $LiFePO_4$ nanoparticles anchored on a three-dimensional graphene aerogel as high-performance positive electrode materials for lithium-ion batteries. J. Power Sources 340 (2017) 40-50.

37. M. Zhang, Z. Sun, T. Zhang, D. Sui, Y. Ma, Y. Chen. Excellent cycling stability with high SnO_2 loading on a three-dimensional graphene network for lithium ion batteries. Carbon 102 (2016) 32-38.

38. X. Xu, Y. Zhou, J. Lu, X. Tian, H. Zhu, J. Liu. Single-step synthesis of PtRu/N-doped graphene for methanol electrocatalytic oxidation. Electrochim. Acta 120

(2014) 439-451.

39. Y. Zhou, X. Xu, B. Shan, Y. Wen, T. Jiang, J. Lu, S. Zhang, D. P. Wilkinson, J. Zhang, Y. Huang. Tuning and understanding the supercapacitance of heteroatom-doped graphene. Energy Storage Materials 1 (2015) 103-111.

40. J. Lu, Y. Zhou, X. Tian, X. Xu, H. Zhu, S. Zhang, T. Yuan. Synthesis of boron and nitrogen doped graphene supporting PtRu nanoparticles as catalysts for methanol electrooxidation. Appl. Surf. Sci. 317 (2014) 284-293.

41. X. Xu, Y. Zhou, T. Yuan, Y. Li. Methanol electrocatalytic oxidation on Pt nanoparticles on nitrogen doped graphene prepared by the hydrothermal reaction of graphene oxide with urea. Electrochim. Acta 112 (2013) 587-595.

42. Z. S. Wu, G. Zhou, L. C. Yin, W. Ren, F. Li, H. M. Cheng. Graphene/metal oxide composite electrode materials for energy storage. Nano Energy. 1 (2012) 107-131.

43. G. Kucinskis, G. Bajars, J. Kleperis. Graphene in lithium ion battery cathode materials: A review. J. Power Sources 240 (2013) 66-79.

44. A. Vu, A. Stein. Multiconstituent synthesis of $LiFePO_4$/C composites with hierarchical porosity as cathode materials for lithium ion batteries. Chem. Mater. 23 (2011) 3237-3245.

45. C. M. Doherty, R. A. Caruso, C. J. Drummond. High performance $LiFePO_4$ electrode materials: Influence of colloidal particle morphology and porosity on lithium-ion battery power capability. Energy Environ. Sci. 3 (2010) 813-823.

46. C. Sun, S. Rajasekhara, J. B. Goodenough, F. Zhou. Monodisperse porous $LiFePO_4$

microspheres for a high power li-ion battery cathode. J. Am. Chem. Soc. 133 (2011) 2132-2135.

47. R. Dedryvère, M. Maccario, L. Croguennec, F. Le Cras, C. Delmas, D. Gonbeau. X-ray photoelectron spectroscopy investigations of carbon-coated Li_xFePO_4 materials. Chem. Mater. 20 (2008) 7164-7170.

48. X. Xu, Z. Hao, H. Wang, J. Liu, H. Yan. Mesoporous carbon derived from Zif-8 for improving electrochemical performances of commercial $LiFePO_4$. Mater. Lett. 197 (2017) 209-212.

Figures and captions

(a) Graphene oxide

(b) Graphene aerogel

(c) LFP-GA precursor
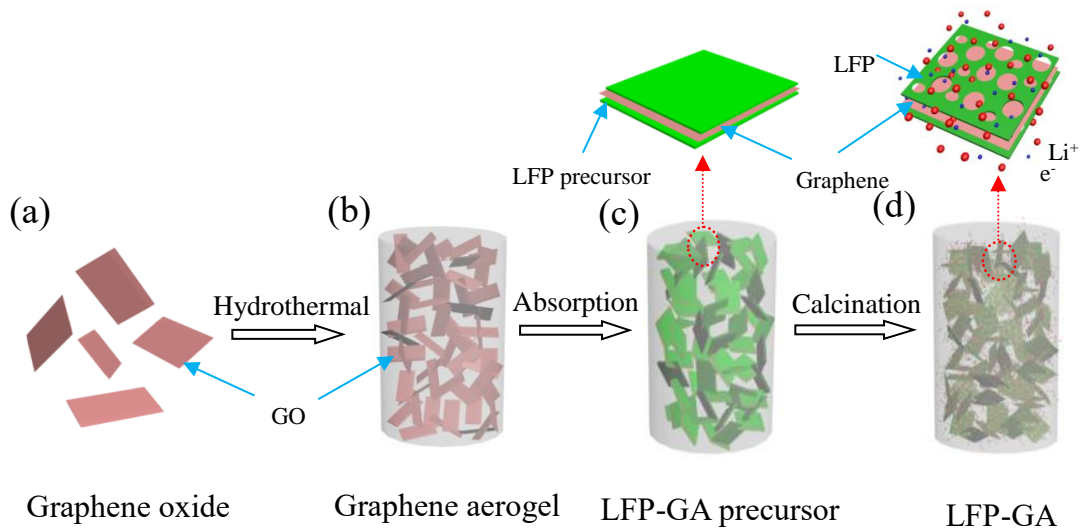
(d) LFP-GA

Figure 1. Schematic illustrations of the formation of LFP-GA: (a) Graphene oxide (GO); (b) Graphene aerogel formed after a hydrothermal treatment of GO and subsequent freeze drying; (c) LFP-GA precursor formed by the adsorption of LFP sol on graphene aerogel and the following gelatification; (d) LFP-GA composite formed by the calcination of the LFP-GA precursor. The enlarged areas of (c) and (d) depicting the fine structure and the mechanisms of facilitated charge transfer as well as Li^+ migration.
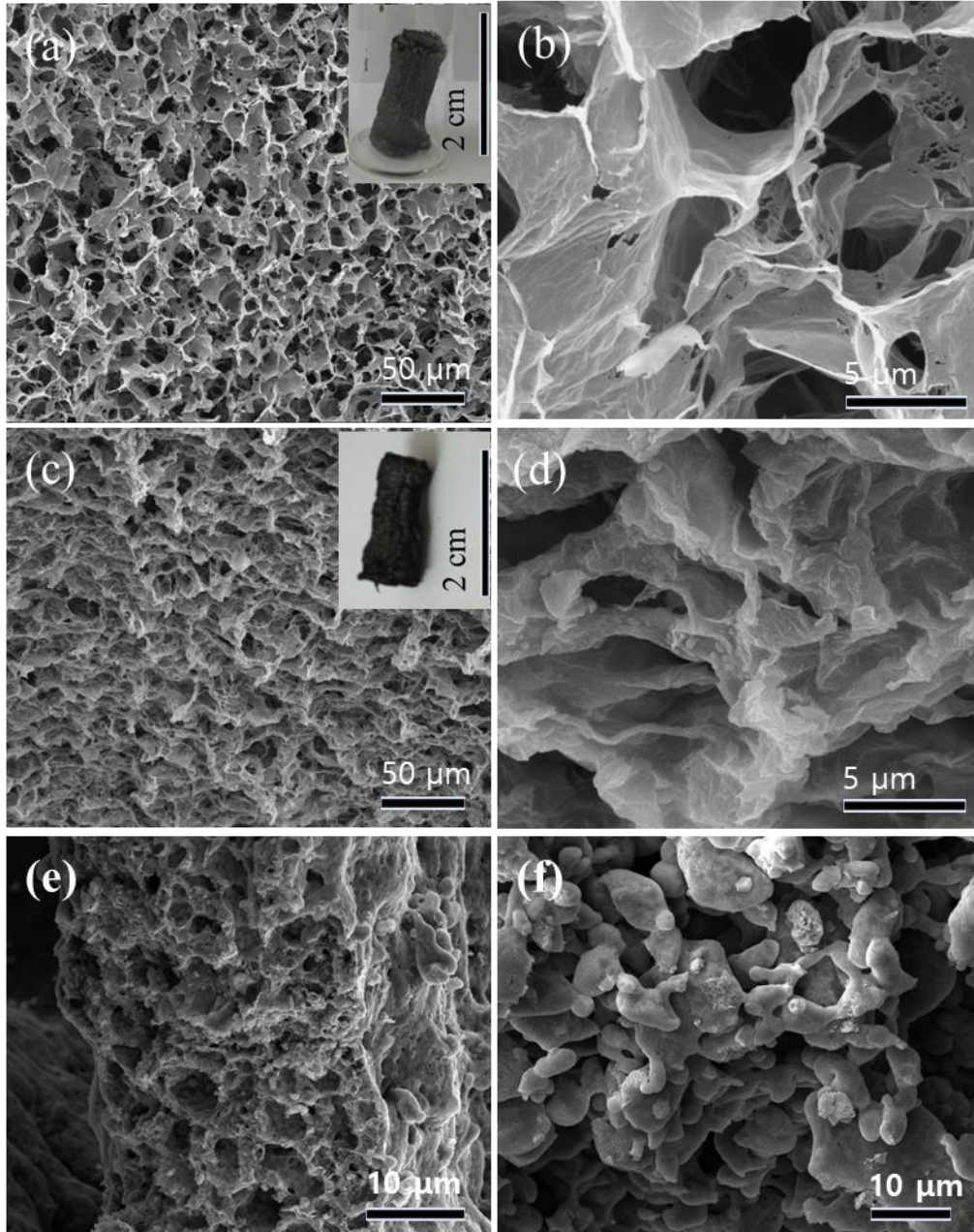
Figure 2. SEM images of (a, b) Graphene aerogel, (c, d) LFP-GA-6%, (e) LFP, (f) LFP-GA-3%.
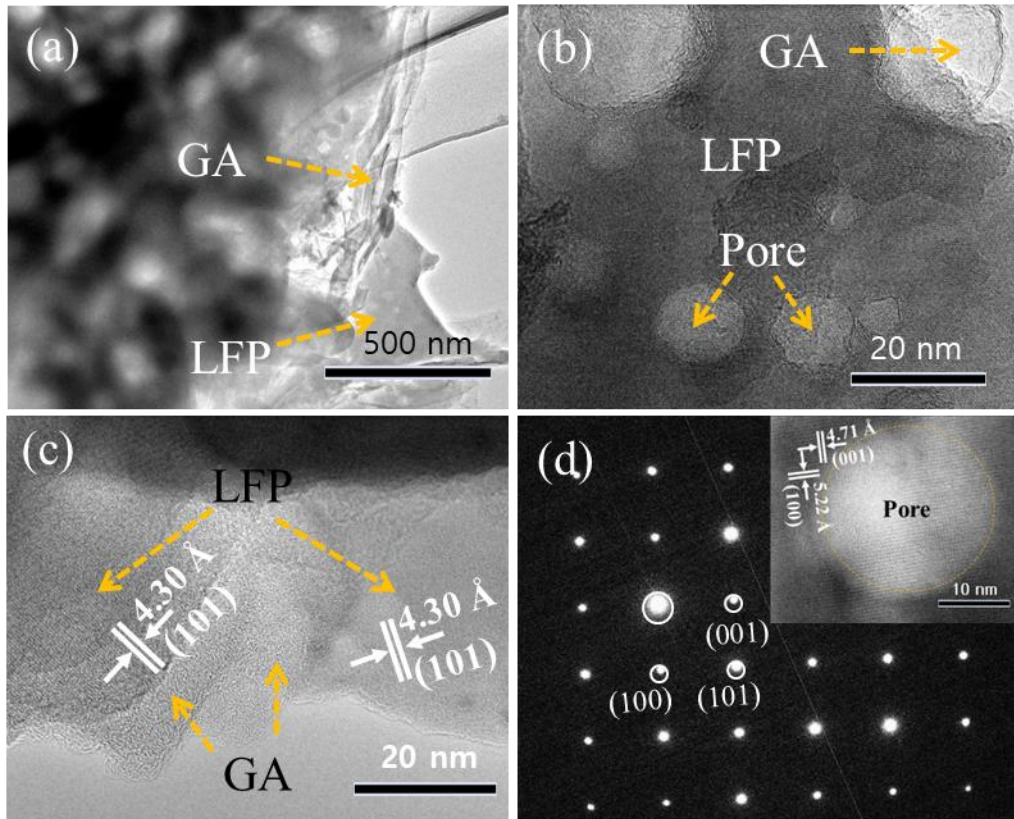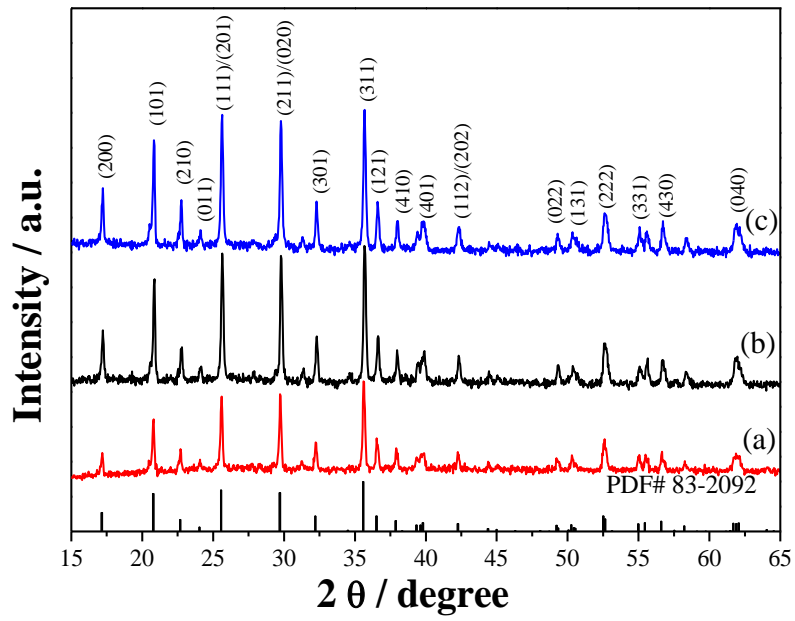
Figure 3. (a, b, c) TEM images and d) Selected area electronic diffraction pattern of LFP-GA-6% (inset: corresponding crystal lattice fingers).

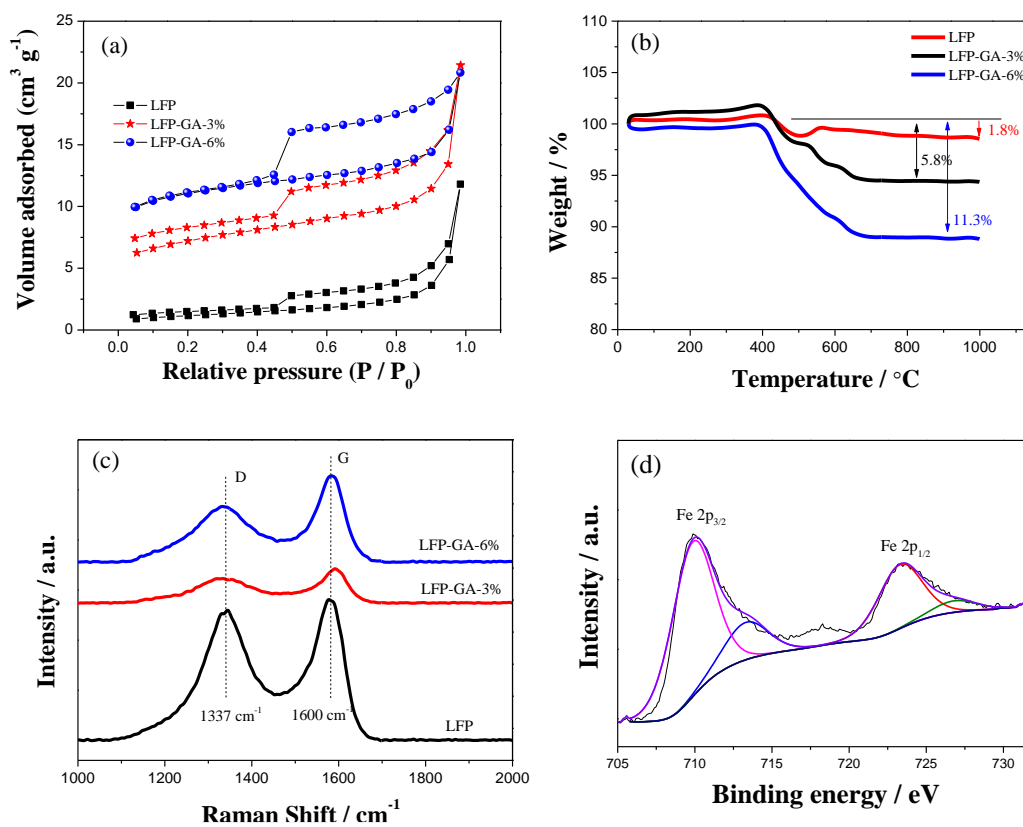**Figure 4.** XRD patterns of (a) LFP, (b) LFP-GA-3% and (c) LFP-GA-6%.
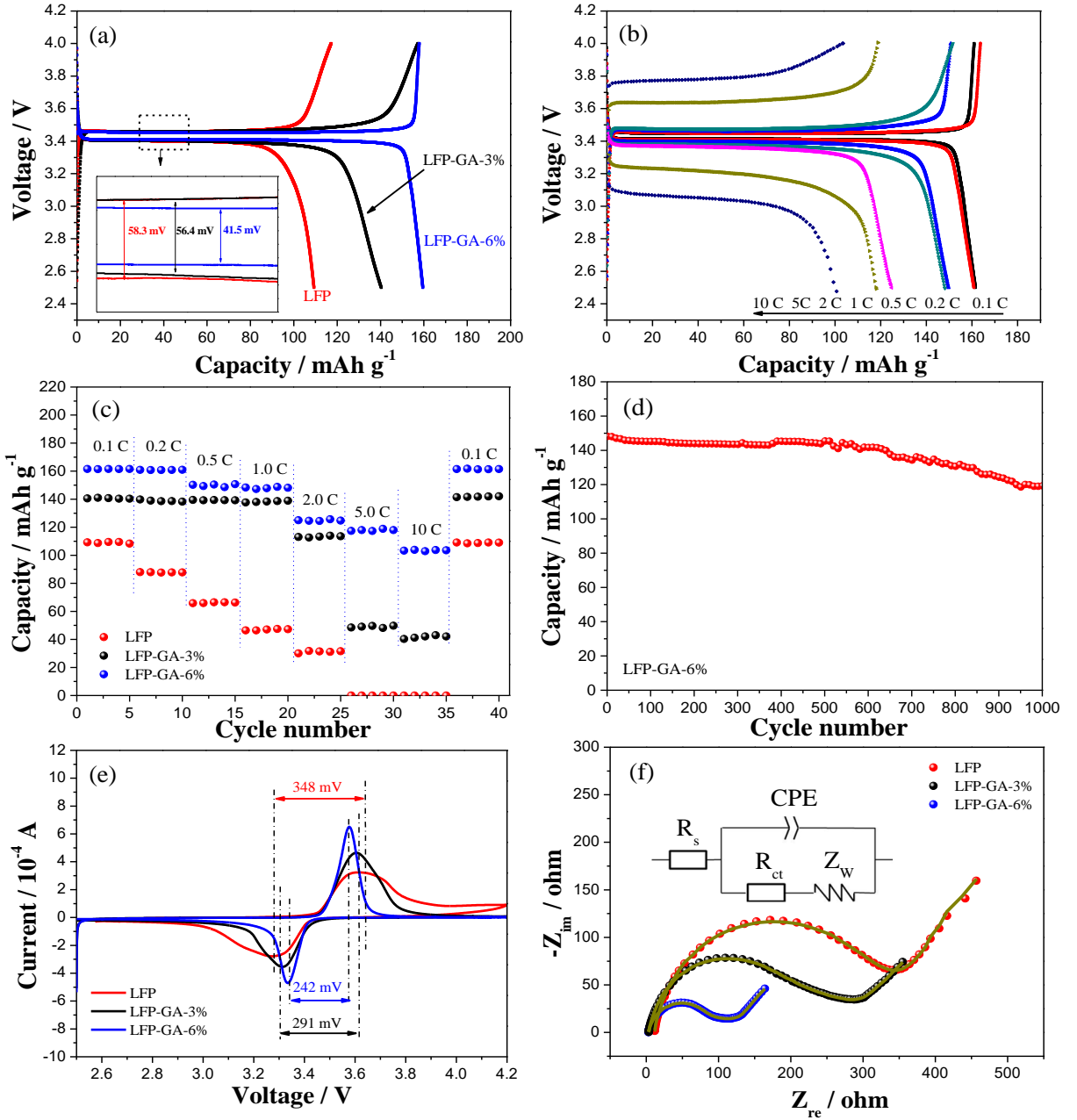
1

2
3

Figure 5. (a) N_2 adsorption/desorption isotherms of LFP, LFP-GA-3% and LFP-GA-

6%; (b) TGA curves of LFP, LFP-GA-3% and LFP-GA-6% heated in air from 30 °C to

1000 °C; (c) Raman spectra of LFP, LFP-GA-3% and LFP-GA-6%; (d) XPS high

resolution Fe 2p spectrum of LFP-GA-6%.

8

Figure 6. (a) Charge-discharge graphs of LFP, LFP-GA-3% and LFP-GA-6% at 0.1 C;

(b) The discharge curves of LFP-GA-6% at 0.1-10 C; (c) The rate capabilities of LFP,

LFP-GA-3% and LFP-GA-6% at 0.1-10 C ; (d) Cycling performances of LFP-GA-6%

during 1000 cycles at 1 C; (e) Comparison of CV results of LFP, LFP-GA-3% and LFP-

GA-6% at 0.1 mV s^{-1}; (f) EIS profiles of LFP, LFP-GA-3% and LFP-GA-6% with

fitting curves by using the inset equivalent circuit.